

Visualisations of coherent centre domains in local Polyakov loops

Finn M. Stokes, Waseem Kamleh, and Derek B. Leinweber

Centre for the Subatomic Structure of Matter, School of Chemistry and Physics, University of Adelaide, SA 5005 Australia

(Dated: May 15, 2022)

Quantum Chromodynamics exhibits a hadronic confined phase at low to moderate temperatures and, at a critical temperature T_C , undergoes a transition to a deconfined phase known as the quark-gluon plasma. The nature of this deconfinement phase transition is probed through analysis of the behaviour of the Polyakov loop, a gauge independent order parameter. We produce visualisations of the structure of centre clusters and analyse percolations of the centre clusters during the deconfinement transition. We observe deconfinement proceeding through the growth of centre clusters. A correlation between the magnitude of the Polyakov loop and the proximity of its phase to one of the centre phases of $SU(3)$ is established. Thus, the size of centre clusters sets the range for the confinement of quarks.

I. INTRODUCTION

Quantum Chromodynamics (QCD) is the gauge field theory that describes the strong interactions of quarks, the constituent particles of hadrons such as protons and neutrons. In QCD, the strong interaction is mediated by a gauge boson known as the gluon. The self-coupling of gluons through the colour charge gives rise to a non-trivial vacuum structure, confining quarks and generating mass through dynamical chiral symmetry breaking.

At a critical temperature, which in vacuum is $T_C \approx 150 - 180$ MeV [10] (around two trillion degrees Kelvin), QCD undergoes a phase transition to a deconfined phase. Above T_C , confinement breaks down, resulting in the formation of a quark-gluon plasma. Understanding the nature of this transition is critical to understanding the formation of hadronic matter in the early universe and the nature of neutron stars. It is also important in interpreting the results of experiments at extremely high energies.

To observe this phase transition in Lattice QCD simulations, one examines the behaviour of a complex-valued observable known as the Polyakov loop which acts as an order parameter. It has an expectation value of zero in the confined phase and a nonzero expectation value in the deconfined phase [5]. As we will observe, this transition occurs through the growth of centre clusters, regions of space where the Polyakov loop prefers a single complex phase associated with the centre of $SU(3)$. It is these clusters that we analyse in this paper.

We will demonstrate deconfinement in the behaviour of the Polyakov loops at T_C and produce and analyse visualisations of the centre clusters that aid in understanding the nature of the phase transition in vacuum. To do this, we develop a custom volume renderer that can correctly visualise the 3D complex field of local Polyakov loops.

II. BACKGROUND

A. Centre Symmetry

In QCD, the gluons are described by the eight gluon fields $A_\mu^a(x)$, which are expressed as the sum

$$A_\mu(x) = A_\mu^a(x) T_a,$$

where T_a are the eight generators of $SU(3)$. The local Polyakov loop is defined to be

$$\begin{aligned} L(\vec{x}) &:= \text{Tr} \left(\mathcal{P} \exp \left[ig \int dx^0 A_0(x) \right] \right) \\ &= \text{Tr} \prod_{t=1}^{N_t} U_0(t, \vec{x}), \end{aligned}$$

where U_0 is the time-oriented link variable on a lattice with lattice spacing a , given by

$$U_\mu(x) = P \exp \left(ig \int_x^{x+\hat{\mu}a} dx^\mu A_\mu(x) \right).$$

Under a local gauge transformation $g(x) \in SU(3)$

$$U_\mu(x) \rightarrow g(x) U_\mu(x) g(x + \hat{\mu}a)^\dagger,$$

so given periodic boundary conditions, the Polyakov loop is invariant under local gauge transformations.

The spatially averaged Polyakov loop is

$$P := \frac{1}{V} \sum_{\vec{x}} L(\vec{x}).$$

By translational invariance, the local Polyakov loop $L(\vec{x})$ has the same vacuum expectation value as the spatially averaged loop P . It is related to the free energy F_q of a static quark by

$$\langle L(\vec{x}) \rangle = \langle P \rangle \propto \exp(-F_q/T).$$

In the confined phase, the free energy of a static quark is infinite, so $\langle L(\vec{x}) \rangle = \langle P \rangle = 0$. In the deconfined

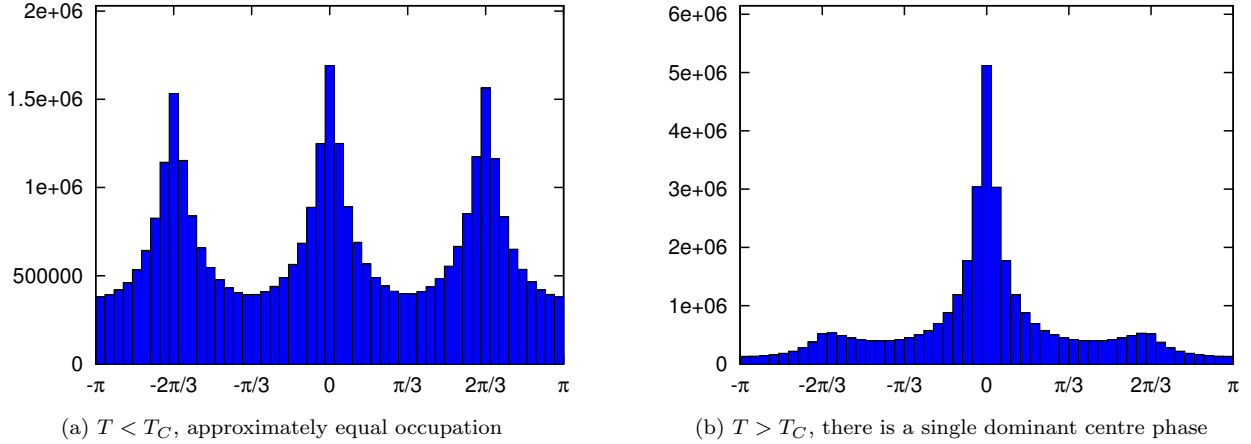


FIG. 1. Histograms of the distribution of complex phases of local loops across a gauge field ensemble, showing differing occupation of the three centre phases.

phase, the free energy of a static quark is finite, so $\langle L(\vec{x}) \rangle = \langle P \rangle \neq 0$ [2]. Thus, the Polyakov loop is an order parameter for confinement.

If the centre of the gauge group

$$C := \{z \in G | zg = gz \forall g \in G\}$$

is non-trivial, then the gauge action is invariant under a centre transformation

$$U_0(t_0, \vec{x}) \rightarrow z U_0(t_0, \vec{x}) \forall \vec{x}, \text{ for some fixed } z \in C, t_0.$$

These transformations form a global symmetry of the theory known as the centre symmetry. Polyakov loops transform non-trivially under centre transformations:

$$L(\vec{x}) \rightarrow z L(\vec{x}),$$

so if the centre symmetry is conserved, $\langle L(\vec{x}) \rangle = 0$ [16]. Thus, the Polyakov loop is an order parameter for the centre symmetry and deconfinement corresponds to a spontaneous breaking of the centre symmetry.

It has been observed [2, 5] that for SU(3) gauge theory below the critical temperature, the complex phase of the local Polyakov loops ($\phi(\vec{x})$ in $L(\vec{x}) = \rho(\vec{x}) e^{i\phi(\vec{x})}$) is distributed evenly between three peaks, one at each of the three centre phases of SU(3) (0, $\frac{2\pi}{3}$, and $-\frac{2\pi}{3}$). We have seen a similar effect in our own simulations as shown in FIG. 1a. As the distribution of $L(\vec{x})$ is uniform about the three centre phases, the expectation value $\langle L(\vec{x}) \rangle$ vanishes. Above the critical temperature, the centre symmetry is spontaneously broken and one of the three peaks becomes dominant. We have replicated this in our simulations as shown in FIG. 1b. As a result, the expectation value $\langle L(\vec{x}) \rangle$ is non-zero.

In full QCD the fermion determinant introduces a preferred phase, causing the peak with a phase of zero to always become dominant above the critical temperature [2]. In pure SU(3) Yang-Mills theory, the direction of this

symmetry breaking is uniformly distributed between the three peaks. In order for the equations in this section to be relevant in an ergodic Markov chain, we would need to remove this remaining symmetry by performing centre transformations to bring each gauge configuration to the same peak.

B. Anisotropic Gauge Action

On the lattice, the temperature T is related to the temporal extent aN_t by $T = \frac{1}{aN_t}$. The volume $V = (aN_s)^3$ depends on the spatial extent of the lattice aN_s . The only way one can change the temperature of an isotropic lattice without changing the volume is by adding or removing lattice sites in the time direction. In order to be able to adjust the temperature in a continuous manner, we instead introduce anisotropy into the lattice, replacing the single lattice spacing a with a spatial lattice spacing a_s and a temporal lattice spacing a_t . In this way we can vary the temperature $T = \frac{1}{a_t N_t}$ while maintaining a constant volume $V = (a_s N_s)^3$ by varying a_t whilst holding a_s fixed.

In order to introduce this anisotropy, we use the anisotropic Iwasaki action [17], which introduces an anisotropy parameter γ_G . This separates the Wilson loops in the plane of two spatial directions from the Wilson loops in the plane of a single spatial and temporal direction. The gauge action is

$$S_G[U] = \beta \left\{ \frac{1}{\gamma_G} \sum_{x, i > j} \{ c_0^s P_{ij}(x) + c_1^s (R_{ij}(x) + R_{ji}(x)) \} \right. \\ \left. + \gamma_G \sum_{x, k} \{ c_0^t P_{k4}(x) + c_1^t R_{k4}(x) + c_2^t R_{4k}(x) \} \right\},$$

where i, j, k are for spatial directions, and $P_{\mu\nu}(x)$ and $R_{\mu\nu}(x)$ are the 1×1 plaquette and 1×2 rectangular loop

in the $\mu - \nu$ plane respectively, β governs the strong coupling, γ_G governs the anisotropy, and the improvement coefficients are [17]

$$\begin{aligned} c_1^s &= c_1^t = c_2^t = -0.331 \\ c_0^s &= c_0^t = 3.648. \end{aligned}$$

C. Hybrid Monte-Carlo

We want to generate an ensemble of gauge field configurations $\{U_i\}$ with probability distribution $\rho(U) = e^{-S_G[U]}$. To do this, we use the Hybrid Monte Carlo (HMC) algorithm [3]. This involves introducing the non-physical constructs Π_μ and τ , the conjugate momenta of U and the simulation time respectively. We then describe the new extended system by the Hamiltonian

$$\mathcal{H}[U, \Pi] = \sum_{x, \mu} \frac{1}{2} \text{Tr} \Pi_\mu(x)^2 + S_G[U].$$

To describe the frame rate of our visualisations, we briefly review the update algorithm. Starting from an initial gauge field configuration U , we apply the following process [9]:

1. Select a random Π from an ensemble distributed according to $\rho(\Pi) \propto e^{-\frac{1}{2} \text{Tr} \Pi^2}$
2. Perform molecular dynamics updates with step size $\Delta\tau$, evolving U_μ to U'_μ and Π_μ to Π'_μ by the following discretised equations of motion (so that $\frac{d\mathcal{H}}{d\tau} \approx 0$):

$$U_\mu(x, \tau + \Delta\tau) = U_\mu(x, \tau) \exp(i\Delta\tau \Pi_\mu(x, \tau))$$

$$\Pi_\mu(x, \tau + \Delta\tau) = \Pi_\mu(x, \tau) - \Delta\tau U_\mu(x, \tau) \frac{\delta S_G}{\delta U_\mu(x, \tau)}$$

3. After $\frac{1}{\Delta\tau}$ updates, providing a trajectory length of 1, we accept or reject the new configuration with probability $\rho = \min(1, e^{-\Delta\mathcal{H}})$, where $\Delta\mathcal{H} = \mathcal{H}[U, \Pi] - \mathcal{H}[U', \Pi']$.

In generating the configurations used in this paper, we used 150 molecular dynamics steps with step size $\Delta\tau = \frac{1}{150}$. When producing visualisations we store the state of the Polyakov loops five times per trajectory in order to make the animation smoother. Of course, these frames are dropped if the configuration is not accepted in step 3.

D. Lattice Spacings and Temperature

The lattice spacings a_s and a_t depend non-trivially on β and γ_G . In order to determine a_s and a_t for a given

TABLE I. The (β, γ_G) pairs and their corresponding temperatures obtained from pure gauge simulations of $24^3 \times 48$ lattices.

β	γ_G	a_s (fm)	a_t (fm)	ξ	T (MeV)
2.620	1.000	0.1016(5)	0.1028(11)	0.988(12)	240(3)
2.645	1.125	0.1014(4)	0.0912(8)	1.112(12)	270(2)
2.670	1.250	0.1019(6)	0.0803(10)	1.245(19)	307(4)
2.695	1.375	0.1014(4)	0.0761(8)	1.335(25)	324(3)
2.720	1.500	0.1002(9)	0.0673(10)	1.489(31)	366(5)
2.740	1.625	0.1007(12)	0.0622(8)	1.618(39)	396(5)
2.760	1.750	0.1019(8)	0.0567(9)	1.796(38)	434(7)

(β, γ_G) pair, we perform a lattice simulation at zero temperature (high temporal extent) and fit the values of the Wilson loops, $W_{\mu\nu}(r, t)$, to the static quark potential

$$V(r) = V_0 + \sigma r - e \cdot \left[\frac{1}{r} \right] + l \cdot \left(\left[\frac{1}{r} \right] - \frac{1}{r} \right),$$

where $\left[\frac{1}{r} \right]$ denotes the tree-level lattice Coulomb term [4].

This ansatz for the static quark potential is sensitive to discretisation effects at extremely small r and noise starts to dominate at large r , so we need a lower and upper cutoff for r .

On an anisotropic lattice, the fit for the space-space loops ($W_{xy}(r, t)$, $W_{xz}(r, t)$, and $W_{yz}(r, t)$) gives a string tension σ_{ss} which is related to the spatial lattice spacing a_s through the physical value $\sqrt{\sigma} = 0.44 \text{ GeV}$. On the other hand, the space-time loops, ($W_{xt}(r, t)$, $W_{yt}(r, t)$, and $W_{zt}(r, t)$) and the time-space loops ($W_{tx}(r, t)$, $W_{ty}(r, t)$, and $W_{tz}(r, t)$) give σ_{st} , which is related to both the spatial and temporal lattice spacings via $\sqrt{a_s a_t}$.

By finding a_s and a_t for a variety of (β, γ_G) pairs, the relationship between β and γ_G necessary to keep a_s constant can be determined. This allows us to choose a set of (β, γ_G) pairs that give us access to a range of temperatures at a fixed volume as shown in TABLE I.

We also found that the renormalised anisotropy,

$$\xi = \frac{a_s}{a_t},$$

is approximately equal to the bare anisotropy, γ_G , in the region we studied.

E. The Polyakov loop

The local Polyakov loop $L(\vec{x})$ is a complex number at each spatial lattice site \vec{x} . We can express it in complex polar form,

$$L(\vec{x}) = \rho(\vec{x}) e^{i\phi(\vec{x})},$$

where $\rho(\vec{x}), \phi(\vec{x}) \in \mathbb{R}$, $\rho(\vec{x}) \geq 0$, and $-\pi < \phi(\vec{x}) \leq \pi$.

Just as the expectation value of L is related to the free energy of a static quark relative to the vacuum by

$$\langle L(\vec{x}) \rangle \propto \exp(-F_q/T),$$

the correlation function $\langle L(\vec{x})L(\vec{y})^\dagger \rangle$ is related to the free energy of a static quark-antiquark pair (a meson) separated by $\vec{x} - \vec{y}$ [16]:

$$\langle L(\vec{x})L(\vec{y})^\dagger \rangle \propto \exp(-F_{q\bar{q}}(\vec{x} - \vec{y})/T).$$

Thus:

1. If $\langle L(\vec{x})L(\vec{y})^\dagger \rangle \neq 0$, then $F_{q\bar{q}}(\vec{x} - \vec{y})$ is finite.
2. If $\langle L(\vec{x})L(\vec{y})^\dagger \rangle = 0$, then $F_{q\bar{q}}(\vec{x} - \vec{y})$ is infinite.

If Polyakov loops cluster into regions near a single centre phase (as we shall see is the case in Section III), we can then conclude the following:

1. If \vec{x} and \vec{y} lie within a single cluster, $\phi(\vec{x}) \approx \phi(\vec{y})$ and

$$\begin{aligned} \langle L(\vec{x})L(\vec{y})^\dagger \rangle &= \left\langle \rho(\vec{x})\rho(\vec{y})e^{i(\phi(\vec{x})-\phi(\vec{y}))} \right\rangle \\ &\approx \langle \rho(\vec{x})\rho(\vec{y}) \rangle \\ &\neq 0. \end{aligned}$$

That is, the phases at \vec{x} and \vec{y} cancel out, and the correlation function is non-zero. Thus, $F_{q\bar{q}}(\vec{x} - \vec{y})$ is finite and quark-antiquark pairs can be separated within a cluster.

2. If \vec{x} and \vec{y} lie within different clusters, $\phi(\vec{x}) \neq \phi(\vec{y})$ in general and hence

$$\langle L(\vec{x})L(\vec{y})^\dagger \rangle = 0$$

That is, independent fluctuations in the phases at \vec{x} and \vec{y} cause the correlation function to average to zero. Thus, $F_{q\bar{q}}(\vec{x} - \vec{y})$ is infinite and quark-antiquark pairs cannot be separated across cluster boundaries.

Therefore, the cluster size has a physical significance, governing the confining scale of the theory and the size of mesons.

Similarly, the correlation function $\langle L(\vec{x})L(\vec{y})L(\vec{z}) \rangle$ is related to the free energy of a static quark triplet (a baryon):

$$\langle L(\vec{x})L(\vec{y})L(\vec{z}) \rangle \propto \exp(-F_{qqq}(\vec{x}, \vec{y}, \vec{z})/T).$$

Again, if the Polyakov loops cluster into regions near a single centre phase, we conclude the following:

1. If \vec{x} , \vec{y} and \vec{z} lie within a single cluster, $\phi(\vec{x}) \approx \phi(\vec{y}) \approx \phi(\vec{z})$ and

$$\begin{aligned} \langle L(\vec{x})L(\vec{y})L(\vec{z}) \rangle &= \left\langle \rho(\vec{x})\rho(\vec{y})\rho(\vec{z})e^{i(\phi(\vec{x})+\phi(\vec{y})+\phi(\vec{z}))} \right\rangle \\ &\approx \langle \rho(\vec{x})\rho(\vec{y})\rho(\vec{z}) \rangle \\ &\neq 0, \end{aligned}$$

as $e^{i3\phi} = 1$ for $\phi = 0, \frac{2\pi}{3}, \frac{-2\pi}{3}$. Thus, $F_{qqq}(\vec{x}, \vec{y}, \vec{z})$ is finite and quark triplets can be separated within a cluster.

2. If (for example) \vec{x} and \vec{y} lie within different clusters, $\phi(\vec{x}) \neq \phi(\vec{y})$ in general and hence

$$\langle L(\vec{x})L(\vec{y})L(\vec{y}) \rangle = 0$$

That is, independent fluctuations in the phases at \vec{x} , \vec{y} , and \vec{z} cause the correlation function to average to zero. Thus, $F_{qqq}(\vec{x}, \vec{y}, \vec{z})$ is infinite and quark triplets cannot be separated across cluster boundaries.

Thus, quarks are confined to within the scale of a single cluster. Below the critical temperature, when the clusters have a limited finite size, this results in confinement. From a model perspective, this scale governs the size of the quark core of hadrons which is dressed by the mesonic cloud. Above the critical temperature, as a single cluster grows to encompass the entire space, the quarks become deconfined [5].

F. Potts Model

The universal properties at finite temperature phase transitions in $(3 + 1)$ dimensional gauge theories are related to those in 3-dimensional spin models [11, 16]. Thus, it is of interest to compare the behaviour of the Polyakov loops in QCD with the three dimensional 3-state Potts model [8], a generalisation of the Ising spin model. In the 3-state Potts model, each lattice site can assume one of three spin directions and these form spin aligned domains. After the phase transition, one direction dominates the space, just as in the QCD deconfinement transition. Thus, the Potts model is a candidate for a simplified model of deconfinement.

The 3-state Potts model for a three dimensional lattice of points $\vec{x} \in \mathbb{L} \subset \mathbb{Z}^3$ with spin $\sigma(\vec{x}) = 1, 2$ or 3 at each lattice site is described by the partition function

$$Z = e^{-\beta E[\sigma]},$$

where

$$E[\sigma] = \sum_{\vec{x}} \sum_i \delta_{\sigma(\vec{x}), \sigma(\vec{x}+\hat{i})},$$

is summed over the points of the lattice and the three spatial directions, \hat{i} is the unit vector in the positive i direction, and $\delta_{j,k}$ is the Kronecker delta. That is, $E[\sigma]$ is the total number of spin-aligned nearest-neighbor pairs. Here, $\beta = J/k_B T$ is the inverse temperature in natural units.

We can simulate this using the Metropolis-Hastings algorithm [6] to study the behaviour of spin-aligned domains near the critical temperature and compare it to the behaviour of centre clusters in QCD near T_C .

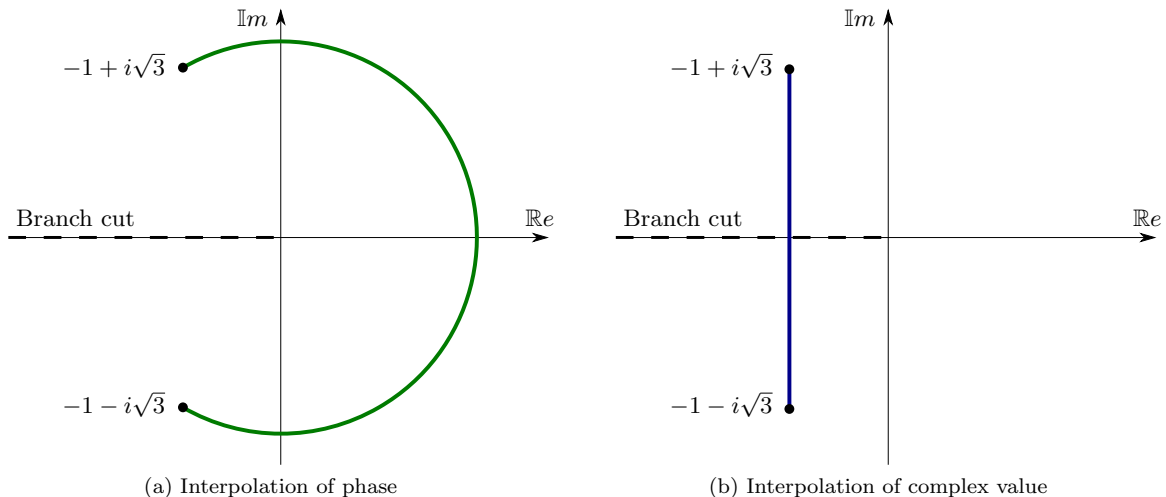


FIG. 2. Diagrams showing path followed by different interpolation methods.

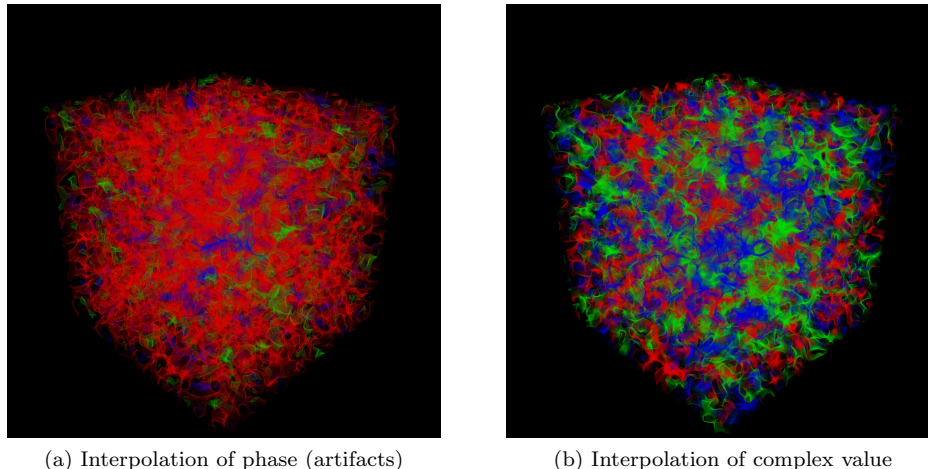


FIG. 3. (Colour online) Visualisations demonstrating the (red) artifacts produced by the incorrect phase interpolation on the left. On the right, the correct complex interpolation shows an equal centre phase distribution.

III. RESULTS

A. Visualisation

In order to analyse the behaviour of the Polyakov loops at the critical temperature, we generate gauge field configurations on several $24^3 \times 8$ lattices with the same spatial lattice spacing but different temporal spacings, using the parameters described in Section II.

Visualising the Polyakov loop data presents a difficulty. Most visualisation software that has the ability to render volumetric data takes in a three dimensional grid of real values and uses trilinear interpolation to fill in the gaps. However, if we try to do this with the complex phase of our Polyakov loop values (with a branch cut at π), we find that the interpolation has problems near the branch cut. For example, if two adjacent data points have complex values $-1 \pm i\sqrt{3}$ (corresponding to complex phases of $\phi = \pm\frac{2\pi}{3}$) then interpolating the phase linearly between

the two points takes it through $\phi = 0$ as in FIG. 2a, rather than crossing the branch cut as in FIG. 2b. This behaviour is incorrect and produces artifacts in the final image that look like thin shells or films between regions of transparency. This leads to much more red (corresponding to $\phi = 0$) than either of green or blue ($\phi = \frac{2\pi}{3}$ and $\phi = -\frac{2\pi}{3}$ respectively) as seen in FIG. 3a.

Instead, we want to directly interpolate the complex numbers and *then* calculate the phase, resulting in the phase going directly between the two endpoints, across the branch cut as in FIG. 2b. This results in a significantly different visualisation as seen in FIG. 3b.

To circumvent this problem, we have developed a custom volume renderer for complex valued scalar fields. The details of the rendering algorithm are given in the Appendix. There we present two ways of visualising the centre clusters, one based on proximity of $\phi(\vec{x})$ to one of the three centre phases and one on the magnitude $\rho(\vec{x})$.

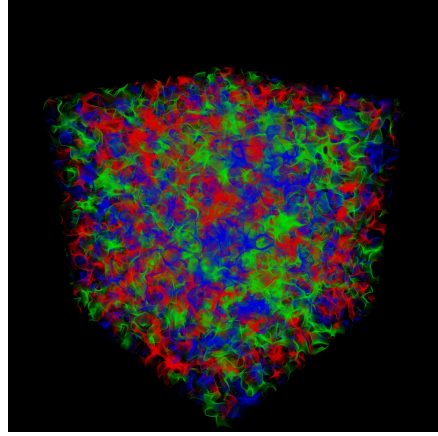
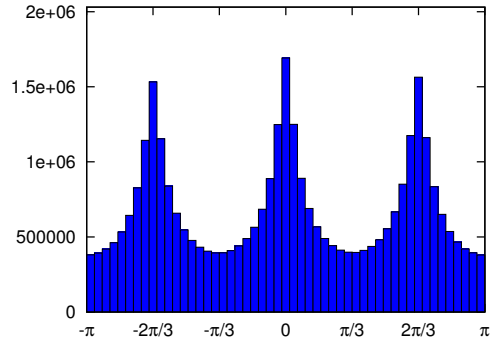


FIG. 4. (Colour online) Histogram of the phase $\phi(\vec{x})$ and a visualisation of the centre clusters in the local Polyakov loop values at $T = 0.78(1) T_C$. All three centre phases are present in small clusters with approximately equal density.

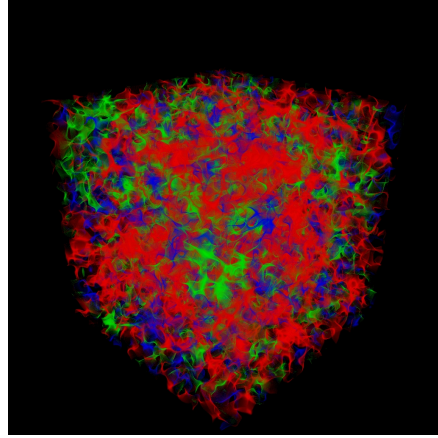
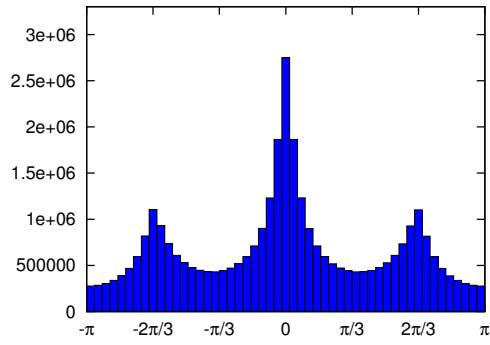


FIG. 5. (Colour online) Histogram and visualisation as in FIG. 4 at $T = 1.00(2) T_C$. A single (red) phase is beginning to dominate, signalling deconfinement.

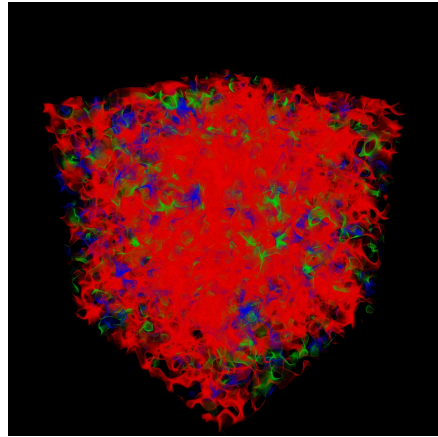
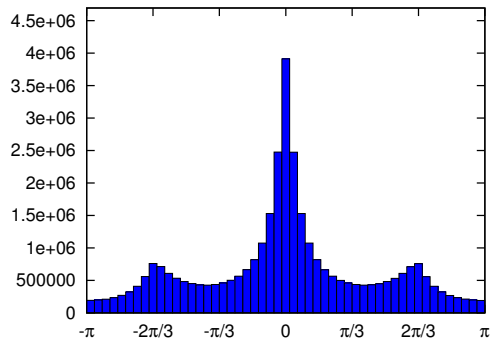


FIG. 6. (Colour online) Histogram and visualisation at $T = 1.19(2) T_C$. A single (red) cluster dominates the entire space.

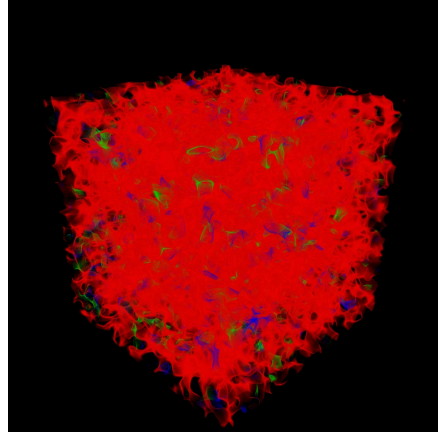
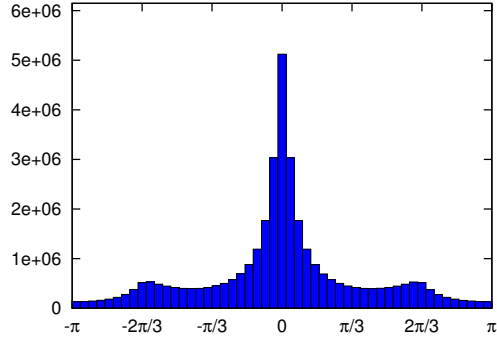


FIG. 7. (Colour online) Histogram and visualisation at $T = 1.41(3) T_C$. The same (red) phase is still dominant.

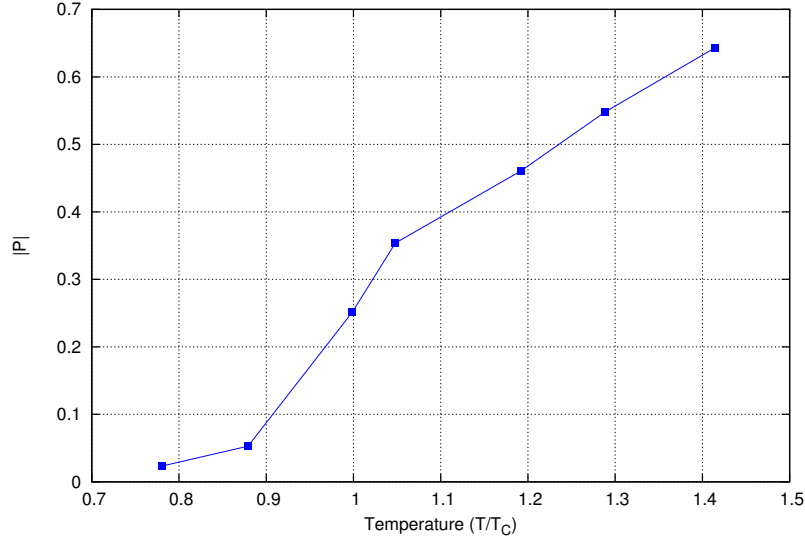
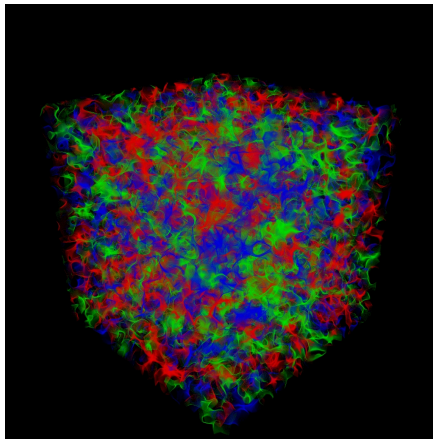
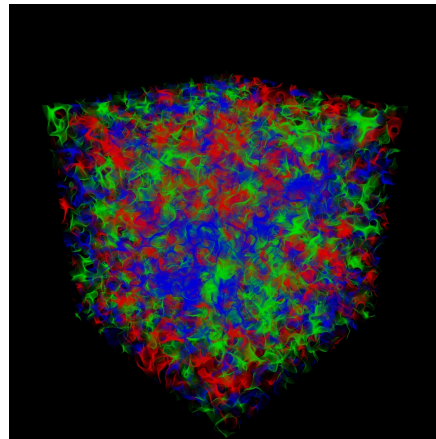


FIG. 8. Variation of the ensemble average of the modulus of the spatially averaged Polyakov loop with temperature. The finite-volume crossover for our results is consistent with the determination of T_C [7].



(a) Thermalised configuration



(b) After one unit HMC trajectory

FIG. 9. (Colour online) Evolution of centre clusters with simulation time at $T = 0.78(1) T_C$.

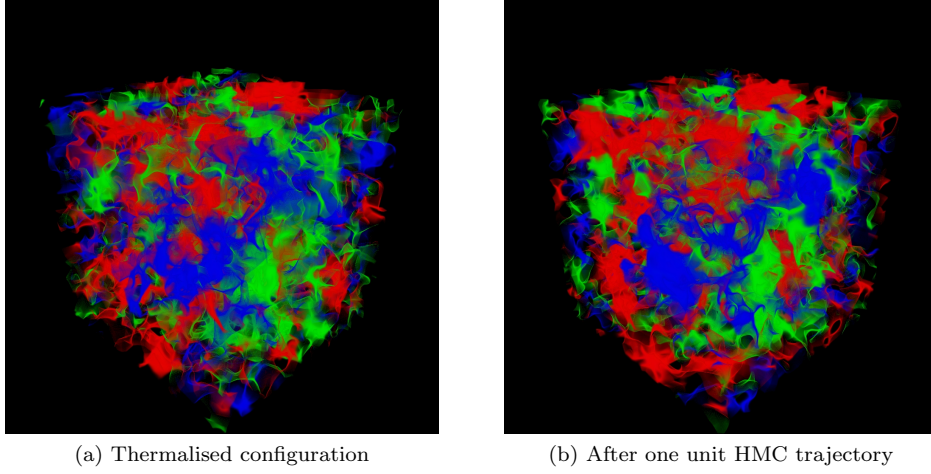


FIG. 10. (Colour online) Evolution of centre clusters with simulation time at $T = 0.78(1) T_C$. Four sweeps of stout-link smearing are applied to the gauge links prior to calculating the Polyakov loops.

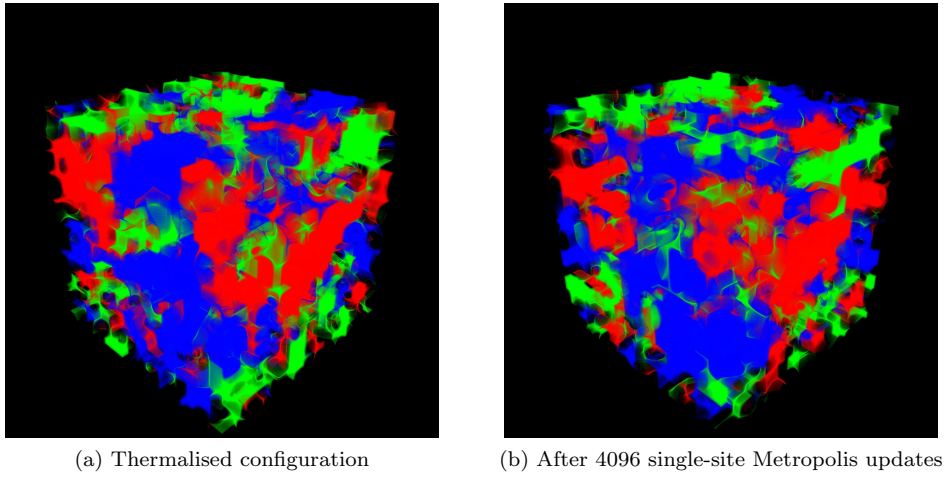


FIG. 11. (Colour online) Evolution of spin-aligned domains in the three dimensional 3-state Potts model at $\beta = 0.55$ on a 16^3 lattice.

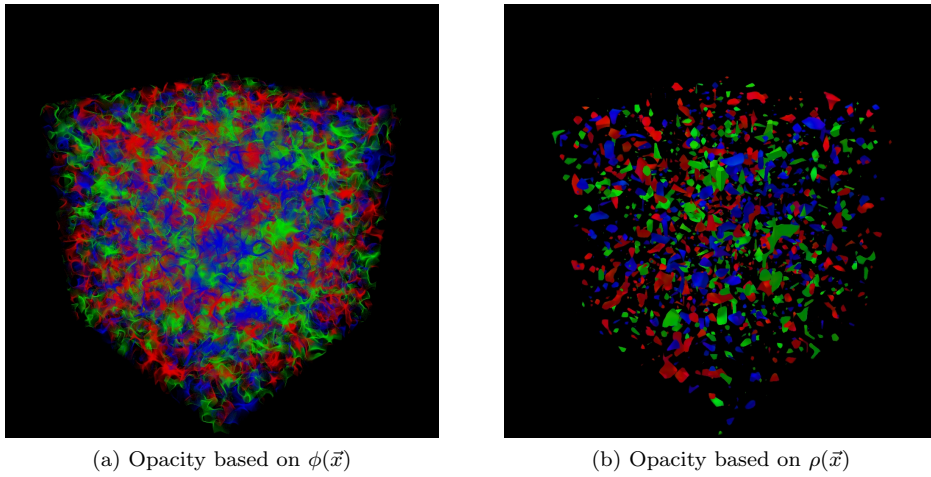
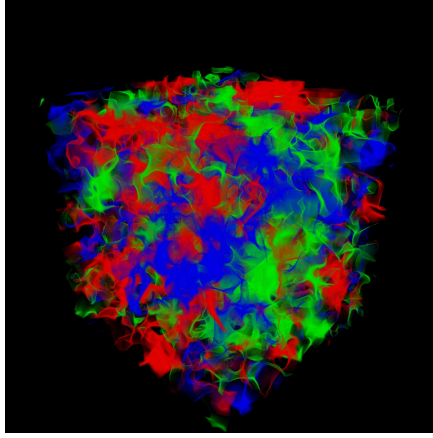
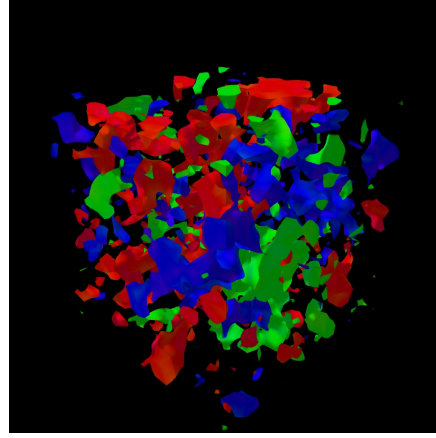


FIG. 12. (Colour online) Comparison of complex phase $\phi(\vec{x})$ and magnitude $\rho(\vec{x})$ clusters at $T = 0.78(1) T_C$.

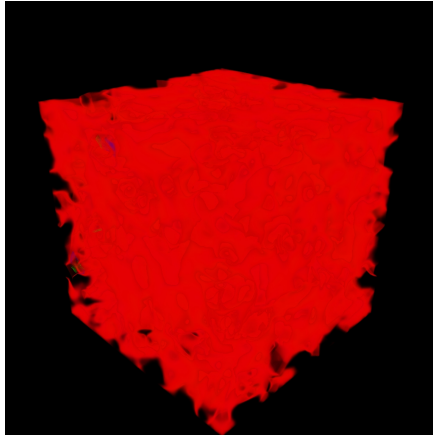


(a) Opacity based on $\phi(\vec{x})$

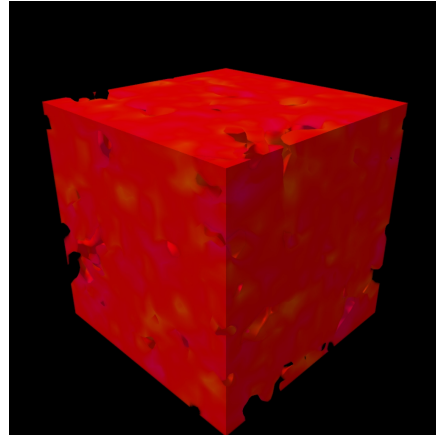


(b) Opacity based on $\rho(\vec{x})$

FIG. 13. (Colour online) Comparison of phase $\phi(\vec{x})$ and magnitude $\rho(\vec{x})$ clusters at $T = 0.78(1) T_C$ after four sweeps of stout-link smearing



(a) Opacity based on $\phi(\vec{x})$



(b) Opacity based on $\rho(\vec{x})$

FIG. 14. (Colour online) Comparison of phase $\phi(\vec{x})$ and magnitude $\rho(\vec{x})$ clusters at $T = 1.41(3) T_C$ after four sweeps of stout-link smearing.

B. Critical Temperature

From Iwasaki *et al.* [7], the critical temperature for a $20^3 \times 4$ lattice with Iwasaki glue is at $\beta = \beta_C = 2.2865(9)$ which corresponds to the critical time oriented spacing $a_C = 0.1603(3)$ providing $T_C = 307(1)$ MeV.

Four animations are available online at the URL provided in Ref. [1]. Two different rendering techniques are presented. As discussed in the Appendix, these include rendering based on the proximity of $\phi(\vec{x})$ to one of the three centre phases of SU(3) and rendering based on the magnitude $\rho(\vec{x})$. Each are rendered from the original configurations as well as configurations smoothed with four sweeps of stout link smearing as discussed in greater detail below.

The animations reveal the percolation of centre clusters as a function of the HMC simulation time, with five frames per unit trajectory. We commence with a thermalised configuration at $T = 240(3)$ MeV or $T/T_C = 0.78(1)$. To show the nature of the HMC updates, we present 750 frames corresponding to 150 HMC trajectories. At our framerate of 25 frames per second, this lasts 30 seconds. A snapshot of the centre clusters at this temperature is provided in FIG. 4. On the left-hand plot, a histogram of the distribution of the phases of the Polyakov loops across a gauge field ensemble at this temperature shows that all three centre phases, observable as peaks in the histogram, are approximately equally occupied, signalling confinement. The right-hand plot shows a single frame from the animation, in which the three centre-phase peaks observed in the histogram correspond to blue (left), red (centre), and green (right). All three centre phases are present in small clusters with approximately equal density.

At this point (0:30 in the animation), the temperature is increased to $T = 307(4)$ MeV or $T/T_C = 1.00(2)$ and the response of the gauge field is illustrated in the animations. FIG. 5 shows the red centre phase becoming dominant with the other two beginning to be suppressed, signalling the onset of deconfinement. This suggests that our data is consistent with the Iwasaki value for the critical temperature [7]. In the animation, we can see that the three centre phases start out equally dominant and fluctuate in size until the red clusters come to dominate.

After 600 HMC trajectories or 120 seconds, at 2:30 in the animation, the configuration has responded to the temperature change and we increase the temperature again, this time to $T = 366(5)$ MeV or $T/T_C = 1.19(2)$. At this temperature, the animation shows that the red clusters continue to grow, occupying almost the entire space. This can be seen in the snapshot provided in FIG. 6.

After 250 more HMC trajectories or 50 seconds, at 3:20 in the animation, we increase the temperature again, to $T = 366(5)$ MeV or $T/T_C = 1.41(3)$. At this temperature, the red phase remains dominant in the animation and the other two phases are suppressed even further. FIG. 7 provides a snapshot at this temperature, showing

the red phase almost completely dominant. We show 250 HMC trajectories at this temperature over the remaining 50 seconds of the animation.

C. Ensemble Average

When we calculate the ensemble average of $|P|$, $\langle |P| \rangle$, at each of the temperatures we are examining, we expect to see the value below T_C to be approximately zero and the value above T_C to be non-zero. We expect the transition at $T = T_C$ to become discontinuous as the volume is increased (as the transition in the infinite volume limit is first order [5]). Finite volume effects result in a crossover. FIG. 8, produced by averaging $|P|$ across an ensemble of gauge field configurations at each temperature displays this behavior.

D. Monte-Carlo Evolution

By examining visualisations of the centre clusters on gauge field configurations separated by a single HMC trajectory, we can observe the evolution of the centre clusters with simulation time. We can see that over the course of a single unit trajectory, the small scale structure of the loops changes significantly, as shown in FIG. 9.

To investigate the larger scale behaviour, we remove the small scale noise by performing four sweeps of stout-link smearing [19] prior to calculating the Polyakov loops. The results are illustrated in FIG. 10. In these visualisations, we see that over the course of one trajectory, the centre clusters are slowly moving, with some change around the boundaries of the clusters.

This is consistent with the behaviour of spin-aligned domains in the three dimensional 3-state Potts model [8] just below the critical temperature under Metropolis-Hastings algorithm simulations, as seen in FIG. 11.

We can also see that once a particular centre phase comes to dominate the space, that phase remains dominant for the rest of the simulation. That is, the dominant phase is highly stable under the process of HMC updates.

If we use the alternate rendering style based on the magnitude $\rho(x)$, we can see that peaks in the magnitude lie approximately within the centre clusters, as shown in FIG. 12. The magnitude peaks are each coloured corresponding to a single centre phase and they appear to line up with peaks in the corresponding phase based visualisation. However it is not necessarily clear that each centre cluster corresponds to a peak in the modulus, $\rho(\vec{x})$.

In order to look more closely at the correlation between these clusters, we again perform four sweeps of stout-link smearing, making it easier to observe larger scale structures. When we do this, it becomes clear that there is an approximate one-to-one relationship between the peaks in the magnitude $\rho(\vec{x})$ and the proximity of $\phi(\vec{x})$ to a centre phase. This is illustrated in FIG. 13.

These peaks in the magnitude of the local Polyakov loops mean that the free energy of a quark-antiquark pair is minimised in the core of a centre cluster. Thus we have a confining potential with local minima at the cores of centre clusters. Below the critical temperature the peaks are sharp so the gradient of the potential is steep, resulting in a strong restoring force confining the quarks to the core of the cluster. Above the critical temperature, as seen in FIG. 14, the peaks become much broader so the gradient is significantly smaller and the restoring force is greatly reduced.

IV. CONCLUSION

We simulated SU(3) Yang-Mills theory on anisotropic $24^3 \times 8$ lattices with the Iwasaki gauge action, considering renormalised anisotropy ranging from $\xi \approx 0.99$ to $\xi \approx 1.80$ with a spatial lattice spacing of $a_s \approx 0.1$. We explored temperatures ranging from $0.78(1)T_C$ to $1.41(3)T_C$. Our focus is on the structure and evolution of centre clusters associated with Polyakov loops.

In doing so, we developed a volume rendering program that correctly deals with the interpolation of three dimensional complex fields such as the local Polyakov loop, and clearly displays their phase (and/or absolute value).

In the visualisations produced in this study, we observed clusters of sizes of order 0.5 fm, setting the scale for the size of hadrons in QCD. The cluster behavior is consistent with that of spin aligned domains in the three dimensional 3-state Potts model. This supports the idea that the phase transition is comparable to the percolation of a three state spin system.

We also observe a one to one correspondence between peaks in the absolute value of local Polyakov loops and the locations of centre clusters. These peaks are sharp below the critical temperature. Through considerations of the free energy of multi-quark systems, this results in a minimum of the quark-antiquark potential in the core of each centre cluster with a steep gradient resulting in a strong restoring force confining the quarks within the cluster. Above the critical temperature the peak structure becomes smooth and the region covered by the domain becomes large. When averaged over an ensemble, any remaining fluctuations in the Polyakov loops are smoothed out and the restoring force becomes negligible. In this way, quarks become deconfined.

Appendix: Visualisation

1. Algorithm

In order to perform the visualisation, we use a ray-traced volume renderer. For each pixel in the final image, a single ray is traced out directly away from the viewer through the volume to be rendered, accruing colour and opacity based on the volumetric data.

Given a RGB (red, green, blue) colour vector $C^{vol}(\vec{x})$ and an opacity $\alpha^{vol}(\vec{x})$ at every point \vec{x} in the volume, we accrue colour and opacity along a ray $\vec{x}(z)$ ($0 \leq z \leq 1$, where $\vec{x}(0)$ is the point where the ray enters the volume and $\vec{x}(1)$ the point where it exits) by the differential equations,

$$\begin{aligned} \frac{d\alpha^{ray}(z)}{dz} &= (1 - \alpha^{ray}(z)) \alpha^{vol}(\vec{x}(z)) , \\ \frac{dC^{ray}(z)}{dz} &= (1 - \alpha^{ray}(z)) C^{vol}(\vec{x}(z)) . \end{aligned}$$

To solve these differential equations, we use Euler's method, with a finite step size Δz [14]:

$$\begin{aligned} \alpha_{n+1}^{ray} &= \alpha_n^{ray} + \Delta z (1 - \alpha_n^{ray}) \alpha^{vol}(\vec{x}(z_n)) , \\ C_{n+1}^{ray} &= C_n^{ray} + \Delta z (1 - \alpha_n^{ray}) C^{vol}(\vec{x}(z_n)) . \end{aligned}$$

In order to perform these calculations, we use OpenGL [12], a 2D and 3D graphics API that allows us to leverage the powerful hardware available in modern GPUs which is designed specifically for rendering graphics. OpenGL provides a flexible graphics processing pipeline which for our purposes consists of a vertex shader followed by a fragment shader. The vertex shader takes in information about the position and shape of three dimensional objects to be rendered and transforms them into the two dimensional space of the screen. The fragment shader runs once for each pixel on the screen, taking information about the polygon visible at that point from the vertex shader and determining the colour the pixel should be.

In our particular case, we adapt a technique by Kruger and Westermann [13] which involves repeatedly rendering a single cube with a sequence of different shader pairs. The vertex shader is the same every time and performs a simple transformation on the cube and calculates the mapping between points on the surface of the cube and points in the volume data that is being rendered. We then have three different fragment shaders that are run in sequence to produce the desired output. A feature that we make extensive use of in order to store interim data is rendering to a framebuffer, an image in memory that serves as a virtual screen, allowing us to store the result of one fragment shader and then use it in a later shading run.

The first fragment shader is run with only the outside faces of the cube visible, so the vertex shader gives the coordinates of the point a ray cast through the current pixel would enter the volume. We store these directly in the red, green, and blue channels of a framebuffer. We then run the second shader with only the inside faces of the cube visible, so the vertex shader gives the coordinates of the point the ray would leave the volume. We then access the entry coordinates from the framebuffer and calculate the direction and length of the ray inside the volume and store them in the red, green, blue, and alpha channels of a new framebuffer.

We can then use a more complicated fragment shader to preform the integration, indexing into a 3D texture

containing the volume data and calculating $C^{vol}(\vec{x})$ and $\alpha^{vol}(\vec{x})$ at each step. By setting the interpolation mode on the texture, we can tell OpenGL to automatically and efficiently perform trilinear interpolation on the data.

By transforming the cube, we can transform the volume being rendered. Thus we perform standard OpenGL model/view and projection transformations on the cube to place the volume in the centre of the screen with perspective and continuously rotate it so that it is possible to see all sides of the volume and observe the 3D structure it contains.

We can then load the pixel data produced by the GPU back into main memory and convert it into a range of formats for later use. In particular, we use DevIL[18] to convert a single frame into a static image, or we use FFmpeg[15] to combine a sequence of frames into a video.

2. Optimisation

Implementing this algorithm naively is rather inefficient for all but the most sparse data sets, as much of the volume is obscured by opaque or nearly opaque regions and has little to no effect on the final image. In order to eliminate this inefficiency, we introduce early ray termination, that is we stop integrating rays once they reach a certain opacity threshold.

We do this by introducing another fragment shader that writes to the depth buffer without changing the colour or opacity. The depth buffer is a special texture used by OpenGL to determine what geometry should be obscured by other geometry. If the opacity has reached a certain threshold, our shader writes the minimum possible value to the depth buffer, effectively terminating the ray.

This shader is then interleaved with the integrating shader, which writes to a framebuffer to store its interim result. This method is also used to stop integrating rays that have left the volume, simply by setting their opacity to 1 if they are outside the volume (equivalent to hitting a solid black backdrop).

In order to maximise efficiency, the integrating shader performs batches of several steps at a time, starting from zero opacity and colour. The result is then appended to the previously calculated integration by using OpenGL blending with the blending mode set to

$$\alpha \rightarrow \alpha + (1 - \alpha)\alpha_{new} ,$$

$$C \rightarrow C + (1 - \alpha)C_{new} .$$

This tells OpenGL how to mix the new colour produced by the fragment shader (C_{new} and α_{new}) with the current

value of the render target (C and α). We can show that combining batches of integration in this way is equivalent to integrating the entire ray in a single batch.

3. Rendering Styles

In this particular case, we take the local Polyakov loops defined at each lattice site and, using trilinear interpolation, get a complex field $L(\vec{x})$ defined everywhere on the volume. We then calculate the complex phase of the loops and the distance to the closest centre phase:

$$\phi(\vec{x}) = \arg(L(\vec{x})) ,$$

$$\Delta\phi(\vec{x}) = \min \left(|\phi(\vec{x})| , \left| \phi(\vec{x}) - \frac{2\pi}{3} \right| , \left| \phi(\vec{x}) + \frac{2\pi}{3} \right| \right) .$$

We then define $C^{vol}(\vec{x})$ and $\alpha^{vol}(\vec{x})$ to be

$$C^{vol}(\vec{x}) = \text{hsv} \left(\frac{\phi(\vec{x})}{2\pi}, 1, 1 \right) ,$$

$$\alpha^{vol}(\vec{x}) = \begin{cases} 100(1 - 20\Delta\phi(\vec{x}))^4 & \text{if } \Delta\phi(\vec{x}) < 0.05 \\ 0 & \text{if } \Delta\phi(\vec{x}) \geq 0.05 \end{cases}$$

where hsv maps a colour expressed in HSV (hue, saturation, value) to its RGB representation:

$$\text{hsv}(h, s, v) = \begin{cases} v \cdot (1, 1 - s(1 - 6h), 1 - s) & \text{if } 0 \leq h < \frac{1}{6} \\ v \cdot (1 - s(6h - 1), 1, 1 - s) & \text{if } \frac{1}{6} \leq h < \frac{2}{6} \\ v \cdot (1 - s, 1, 1 - s(3 - 6h)) & \text{if } \frac{2}{6} \leq h < \frac{3}{6} \\ v \cdot (1 - s, 1 - s(6h - 3), 1) & \text{if } \frac{3}{6} \leq h < \frac{4}{6} \\ v \cdot (1 - s(5 - 6h), 1 - s, 1) & \text{if } \frac{4}{6} \leq h < \frac{5}{6} \\ v \cdot (1, 1 - s, 1 - s(6h - 5)) & \text{if } \frac{5}{6} \leq h < 1 \end{cases}$$

This maps $\phi = 0$ ($h = 0$) to red, $\phi = \frac{2\pi}{3}$ ($h = \frac{1}{3}$) to green, and $\phi = \frac{-2\pi}{3}$ ($h = \frac{2}{3}$) to blue.

We also use an alternative rendering style where the colour is still determined in the same way, but the opacity is determined by the absolute value rather than the phase, allowing us to study the relationship between the phase and the absolute value:

$$\alpha^{vol}(\vec{x}) = \begin{cases} 200(|L(\vec{x})|^2 - 0.2) & \text{if } |L(\vec{x})|^2 > 0.2 \\ 0 & \text{if } |L(\vec{x})|^2 \leq 0.2 \end{cases}$$

[1] <http://www.physics.adelaide.edu.au/cssm/lattice/centreclusters>.

[2] J. Danzer, C. Gatteringer, S. Borsanyi, and Z. Fodor. Center clusters and their percolation properties in lat-

- tice QCD. *PoS*, LATTICE2010:176, 2010.
- [3] S. Duane, A. Kennedy, B. J. Pendleton, and D. Roweth. Hybrid monte carlo. *Physics Letters B*, 195(2):216 – 222, 1987.
 - [4] R. Edwards, U. M. Heller, and T. Klassen. Accurate scale determinations for the Wilson gauge action. *Nucl.Phys.*, B517:377–392, 1998.
 - [5] C. Gattringer and A. Schmidt. Center clusters in the Yang-Mills vacuum. *JHEP*, 1101:051, 2011.
 - [6] W. Hastings. Monte carlo sampling methods using markov chains and their applications. *Biometrika*, 57(1):97–109, 1970.
 - [7] Y. Iwasaki, K. Kanaya, T. Kaneko, and T. Yoshie. Scaling in SU(3) pure gauge theory with a renormalization group improved action. *Phys.Rev.*, D56:151–160, 1997.
 - [8] W. Janke and R. Villanova. Three-dimensional three state Potts model revisited with new techniques. *Nucl.Phys.*, B489:679–696, 1997.
 - [9] W. Kamleh, D. B. Leinweber, and A. G. Williams. Hybrid Monte Carlo with fat link fermion actions. *Phys.Rev.*, D70:014502, 2004.
 - [10] F. Karsch. Lattice results on QCD thermodynamics. *Nucl.Phys.*, A698:199–208, 2002.
 - [11] F. Karsch, C. Schmidt, and S. Stickan. Common features of deconfining and chiral critical points in QCD and the three state Potts model in an external field. *Comput.Phys.Commun.*, 147:451–454, 2002.
 - [12] Khronos Consortium. OpenGL. <http://www.opengl.org/>, 2012. [Online; accessed 13-July-2012].
 - [13] J. Kruger and R. Westermann. Acceleration techniques for gpu-based volume rendering. In *Proceedings of the 14th IEEE Visualization 2003*, VIS '03, Washington, DC, USA, 2003. IEEE Computer Society.
 - [14] M. Levoy. Efficient ray tracing of volume data. *ACM Transactions on Graphics*, 9(3):245–261, 1990.
 - [15] Open source community. FFmpeg. <http://ffmpeg.org/>, 2012. [Online; accessed 18-September-2012].
 - [16] B. Svetitsky and L. G. Yaffe. Critical Behavior at Finite Temperature Confinement Transitions. *Nucl.Phys.*, B210:423, 1982.
 - [17] T. Umeda et al. Two flavors of dynamical quarks on anisotropic lattices. *Phys.Rev.*, D68:034503, 2003.
 - [18] D. Woods, N. Weber, and M. Dario. DevIL — a full featured cross-platform image library. <http://openil.sourceforge.net/>, 2009. [Online; accessed 17-October-2012].
 - [19] J. Zhang, P. J. Moran, P. O. Bowman, D. B. Leinweber, and A. G. Williams. Stout-link smearing in lattice fermion actions. *Phys.Rev.*, D80:074503, 2009.